PAPER • **OPEN ACCESS**

Ag and Pt nanoparticle loaded laser induced graphene for enhanced capacitive glucose sensing

To cite this article: Rou Xuan Goh *et al* 2026 *Eng. Res. Express* **8** 035411

Engineering Research Express

OPEN ACCESS

RECEIVED
27 August 2025

REVISED
18 November 2025

ACCEPTED FOR PUBLICATION
2 February 2026

PUBLISHED
13 February 2026

PAPER

Ag and Pt nanoparticle loaded laser induced graphene for enhanced capacitive glucose sensing

Rou Xuan Goh[1,*], **Suhana Mohamed Sultan**[2], **Pei Ling Leow**[3], **Kien Voon Kong**[4], **Khong Wui Gan**[1], **Suan Hui Pu**[1], **Harold M H Chong**[5] and **Ting Yang Ling**[5]

[1] Smart Manufacturing and Systems Research Group, University of Southampton Malaysia, Johor, Malaysia
[2] Computational Nanoelectronics Research Group, Universiti Teknologi (UTM), Johor, Malaysia
[3] Process Tomography and Instrumentation (PROTOM-i) Research Group, Universiti Teknologi (UTM), Johor, Malaysia
[4] Department of Chemistry, National Taiwan University, Taipei City, Taiwan
[5] Sustainable Electronic Technologies Research Group, School of Electronics and Computer Science, University of Southampton, Southampton, United Kingdom
[*] Author to whom any correspondence should be addressed.

E-mail: rxg1a15@soton.ac.uk

Keywords: capacitance, flexible, glucose, laser-induced graphene, sensor

Abstract

Laser-induced graphene (LIG) electrodes have gained interest for non-enzymatic analyte sensing applications due to their low cost, flexibility, and favorable electrochemical properties. In this study, we investigate the effects of Ag and Pt nanoparticle (NP) surface modification on the capacitive glucose sensing performance of LIG electrodes. LIG was fabricated at varying laser fluences and subsequently decorated with different NP loadings to evaluate interfacial capacitance changes in 1 M KCl electrolyte. Electrochemical characterization revealed that a 10 $\mu g\ ml^{-1}$ NP loading concentration yielded the highest sensitivity — 0.0449 and 0.052 mF $(mM{\cdot}cm)^{-2}$ for Ag- and Pt-modified LIG, respectively — with the lowest detection limit of 1.29 μM achieved by Ag-LIG. Although the study is limited to controlled electrolyte conditions without interference or selectivity tests, the results demonstrate a measurable enhancement in glucose sensitivity compared to pristine LIG. These findings support the potential of metal-NP loaded LIG for cost-effective glucose sensing in high-concentration environments such as food fermentation monitoring.

1. Introduction

Glucose sensing is fundamental in the food and beverage industry, where it is essential for monitoring fermentation processes, controlling product quality, and ensuring batch-to-batch reproducibility [1–3]. This is applicable to brewery mashes, dairy fermentations, and other carbohydrate-driven bioprocesses where glucose concentration is both a critical process variable and an indicator of microbial or enzymatic activity. In these scenarios, glucose levels often range in the multi-gram-per-liter regime, far exceeding those typically seen in clinical or biomedical applications.

Despite their widespread use, the enzyme-based amperometric electrodes that dominate industrial glucose sensing face several limitations. This type of biosensor is reliant on biocatalytic layers such as glucose oxidase or dehydrogenase, which provide molecular selectivity through specific redox reactions [4, 5]. However, enzyme-based systems often suffer from poor long-term stability, limited reusability, and fabrication complexity. Their performance degrades under the challenging conditions of industrial processes where elevated ionic strength, high sugar concentrations, temperature variations, variable viscosity, and vigorous chemical cleaning cycles are common. These compromise the accuracy, repeatability, and lifespan of enzyme-based systems, leading to increased operational costs and maintenance demands.

To address these challenges, there has been growing interest in non-enzymatic electrochemical sensors designed for robust and cost-effective industrial operation that leverage nanostructured carbon materials and metallic nanoparticles to enhance analyte sensing without relying on biological recognition elements [6–8].

Among these sensors, laser-induced graphene (LIG) stands out as a particularly attractive electrode material due to its low-cost, mask-free fabrication process, mechanical flexibility, and tunable surface and electronic properties [9–11]. LIG is formed by laser scribing of polymer substrates and features a porous, conductive carbon network that can be tuned by adjusting laser fluence and wavelength, influencing the resulting surface morphology, pore size, and electrical conductivity [12–14].

LIG's compatibility with post-fabrication surface modification offers further opportunities to enhance its performance. The loading of metallic nanoparticles (NPs), such as silver (Ag), platinum (Pt), copper (Cu), and manganese dioxide (MnO_2), onto the LIG surface has been shown to significantly improve electrochemical activity by increasing effective surface area, improving charge transfer kinetics, and introducing catalytic properties [15–18]. Recent studies have further shown that LIG electrodes decorated with NiCo-LDH or Ag NPs can achieve ultralow detection limits and high sensitivity, highlighting the ongoing improvements in non-enzymatic glucose sensors [19, 20]. These enhancements have been explored in the context of supercapacitors, energy storage, health, and environmental sensing [21–23]. However, their application in capacitive, non-enzymatic glucose sensing under high-concentration, industrially relevant conditions remains relatively underdeveloped, despite its potential to deliver reliable and enzyme-free detection platforms.

Recent advances in capacitive glucose sensors such as carbon nanomaterial-based, metal-oxide, and hybrid electrode systems have demonstrated significant improvements in detection limits and selectivity, but these studies largely target biomedical or micromolar-level glucose ranges [23–25]. In contrast, industrial sensing requires a much broader linear range and tolerance to complex samples. Incorporating LIG as a base material for capacitive sensing thus represents a promising approach to developing durable, low-maintenance sensors for industrial fermentation and food processing contexts.

Capacitive sensing offers several advantages for industrial deployment. Contrary to Faradaic techniques that rely on redox reactions and are prone to electrode fouling, capacitive sensing operates in a pseudocapacitive or capacitive-dominant regime, detecting changes in the electrode–electrolyte interface through variations in interfacial capacitance. This approach is energy-efficient and less susceptible to external interference, making it suitable for continuous or in-line monitoring applications. The total interfacial capacitance ($C_{Interfacial}$) includes quantum capacitance (C_Q), Helmholtz layer capacitance (C_H), and diffuse layer capacitance (C_D), typically modelled as a series of capacitors [26–28]:

$$\frac{1}{C_{Interfacial}} = \frac{1}{C_Q} + \frac{1}{C_H} + \frac{1}{C_D}$$

By treating the combined interfacial capacitance as a representation for analyte interaction at the electrode surface, capacitive sensing enables an indirect yet responsive monitoring of glucose adsorption or local concentration changes.

This study builds upon these principles by examining how NP surface modification influences the capacitive response of LIG-based electrodes toward glucose, and how such modifications could contribute to cost-effective, stable, and non-enzymatic sensing in high-concentration environments. Specifically, effects of loading Ag and Pt NPs onto pristine LIG produced by controlled laser induction are investigated. The interfacial capacitance is estimated electrochemically in a fixed 1 M KCl electrolyte, chosen for its high ionic conductivity and relevance to industrial-like conditions. From this, the assessment on how NP type and concentration influence the glucose sensitivity of the LIG electrodes and identify optimal loading conditions that maximize capacitive response is conducted.

While this work does not include analysis of matrix effects such as pH, fouling, or the presence of interfering species, it provides a foundational and reproducible study demonstrating how NP-LIG interfaces can be engineered to enhance interfacial capacitance and sensitivity. The findings highlight the role of surface modification and laser fluence in tuning LIG's morphology and capacitive performance. Future work will focus on incorporating impedance spectroscopy and selectivity testing to better understand long-term stability and cross-sensitivity under realistic process conditions.

By focusing on practical, non-enzymatic capacitive sensing strategies for industrial concentration regimes, this study contributes to the broader goal of developing scalable, low-cost, and robust glucose sensors suitable for food and bioprocessing applications.

2. Experimental

2.1. Materials and reagents

Ag-NP (average particle size of 100 nm, 0.02 mg ml^{-1}) and Pt-NP (average particle size of 30 nm, 0.05 mg ml^{-1}) were purchased from Merck (Sigma Aldrich) and used without further purification. Aqueous

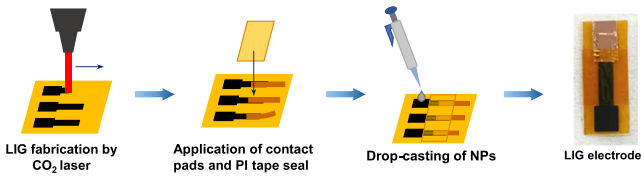

Figure 1. Fabrication process of LIG-based electrode for electrochemical capacitance analysis by laser induction of 50 μm thick PI film.

Table 1. Laser configuration for LIG fabrication.

Electrode	Laser power (W)	Laser fluence (J/cm^2)
L1	8	18.79
L2	12	28.18
L3	16	37.58
L4	18	42.27

electrolyte solutions were prepared by dissolving solid Potassium Chloride (KCl) in DI water. No additional surfactant was added to avoid altering the interfacial properties of the LIG electrode.

2.2. Characterization

Raman spectroscopy (HORIBA XploRA PLUS) in spot-mode was used to confirm the LIG surface characteristics, with a minimum of three replicates per sample to ensure reproducibility, all obtained using 532 nm excitation laser wavelength. The Raman spectrum is expected to show characteristic LIG D-peak at approximately 1350 cm^{-1}, G-peak at 1580 cm^{-1}, and 2D-peak at 2700 cm^{-1} [5, 28]. The D-peak indicates structural defects while the G-peak shows the carbon sp2 bonding which vibrates in-plane. The number of graphene layers stacked in the 'vertical' axis (*c*-axis) is indicated by the peak at the 2D band.

Surface morphology images were obtained using a field emission scanning electron microscope (FESEM) (HITACHI SU8020) at a magnification range from 500 nm to 100 μm. Energy dispersive x-ray spectroscopy (EDS) was performed on the LIG and NP-LIG electrodes to assess the presence of C, O, Ag, and Pt. Across all samples, morphological and compositional uniformity was confirmed in at least three randomly chosen regions.

2.3. Preparation of LIG and NP-LIG

A commercial G690 CO2 IR laser system (LIAOCHENG SHENHUI) at 10.6 μm wavelength is used to form LIG-based electrodes on a commercial polyimide (PI) film of 50 μm thickness, which was purchased and used without further processing. The laser is set to a fixed translational speed of 80 mm s^{-1} and power ranging from 8 W to 18 W, as recorded in table 1. The square sensor electrode (5 mm–by–5 mm) is incorporated with an additional rectangular contact area of 10 mm–by–5 mm at one end for electrical connection. The laser operated with a spot size of 0.5 mm and followed a line-by-line pattern at a step size of 0.2 mm between each laser pass to obtain continuous coverage of LIG. Conductive copper tape was used as the electrical contact and further secured and waterproofed by sealing it with a layer of PI tape. The electrode fabrication method follows that of [29].

Ag and Pt NP dilution was prepared to 6, 10, 14, and 18 μg ml^{-1} by mixing DI water into the concentrated NP stock solutions. The selected range was based on preliminary screening to balance surface coverage and aggregation; concentrations below 6 μg ml^{-1} produced incomplete surface coating, while those above 18 μg ml^{-1} resulted in visible agglomeration and reduced electrochemical stability. For each NP-LIG electrode, 10 μl of the diluted NP solution was drop-cast onto the electrode area, as shown in figure 1, before drying in a glass desiccator jar for approximately 24 h.

Although drop-casting may result in partial NP detachment during immersion into the electrolyte, adhesion was largely maintained by van der Waals and electrostatic interactions between the NP and the porous LIG surface [30]. Future work could explore *in situ* NP incorporation during laser processing to improve bonding strength and reproducibility.

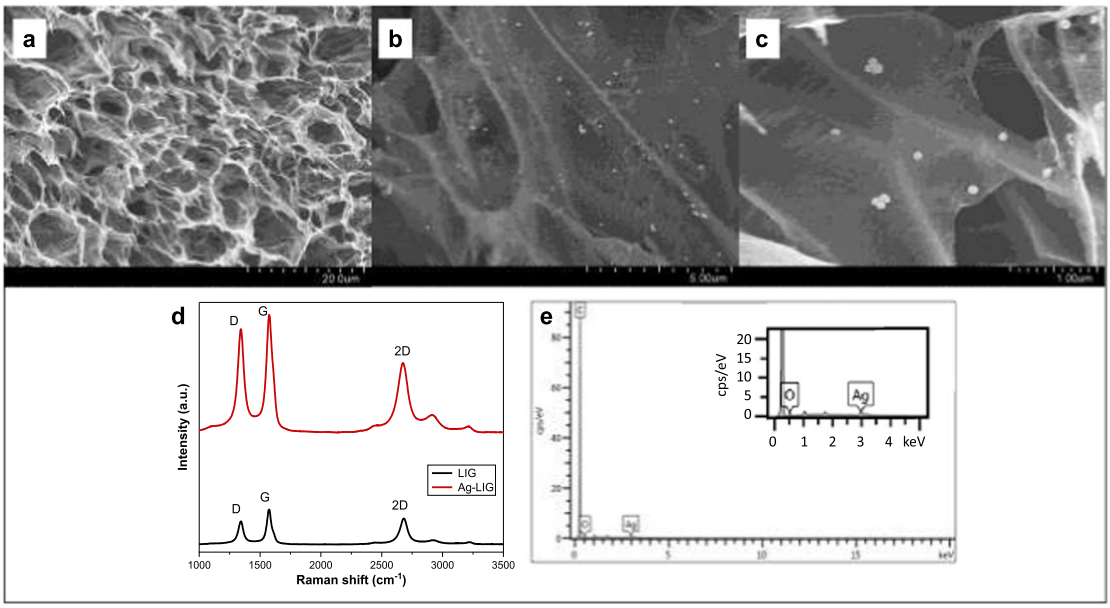

Figure 2. Characterization of the morphology and chemical composition of the Ag-LIG electrode loaded with 10 μg ml^{-1} of Ag NP. (a) FESEM image of electrode surface; (b) FESEM image at higher magnification revealing the distribution of Ag NPs; (c) Further magnification of FESEM showing Ag NPs associated with the walls of the porous LIG; (d) Raman spectra of the Ag-LIG electrode compared to pristine LIG; (e) EDS analysis.

2.4. Electrochemical measurements

Cyclic voltammetry (CV) was performed on a standard three-electrode electrochemical configuration to measure the capacitance of the LIG and NP-LIG electrodes. Ag/AgCl was used as the reference electrode while a 5 mm–by–5 mm platinum plate was used as the counter electrode. The electrolyte chosen was 1 M KCl aqueous electrolyte solution. All electrochemical measurements were obtained through a potentiostat (Autolab PGSTAT101).

CV measurements were run at two scan rates of 5 mV s^{-1} and 50 mV s^{-1} to observe the capacitance responses. The slower scan rate was employed to allow sufficient time for chemical reactions to occur for sensing applications. Conversely, the higher scan rate assessed the rapid capacitive response and operational stability. Each CV curve represents the average of three independent measurements from separately fabricated electrodes, with the standard deviation in capacitance maintained within ±5%.

3. Results and discussions

3.1. LIG formation and presence of NP

FESEM images, figures 2(a)–(c) and 3(a)–(c) of Ag-LIG and Pt-LIG electrodes show similar highly porous structures resembling graphene foam, consistent with typical LIG morphologies. At higher magnifications, NP were observed to be slightly more abundant along the 'walls' of the porous structure due to capillary-driven surface tension effects during solvent evaporation, while still maintaining a uniform distribution across the LIG surface, where the adhesion of Ag and Pt to LIG is likely via van der Waals force and electrostatic interactions [31–33].

The EDS analysis in figures 2(e) and 3(e) confirmed that pristine LIG consisted solely of C and O, while Ag-LIG and Pt-LIG electrodes exhibited additional peaks corresponding to Ag and Pt, respectively, verifying the successful incorporation of NPs. This distribution is likely supported by van der Waals and electrostatic forces . Quantitative EDS data revealed that NP atomic percentages were within ±10% variation across three regions, indicating good deposition uniformity.

The formation of LIG is further confirmed by Raman spectrum, where the peak locations obtained match those of a single-layer graphene [26]. Compared to the pristine LIG, the D, G, and 2D peaks all observed a redshift upon the loading of Ag and Pt NPs in figures 2(d) and 3(d). This is attributed to an increased lattice strain on the LIG structure induced by NP attachment and possible charge transfer between NP and graphene layers [34, 35]. In addition, the spectrum of Ag-LIG has significantly increased intensity, similar to Mu *et al*'s work [36]. The Raman peak ratios for each LIG based electrodes are calculated in table 2. The I_D/I_G ratio for

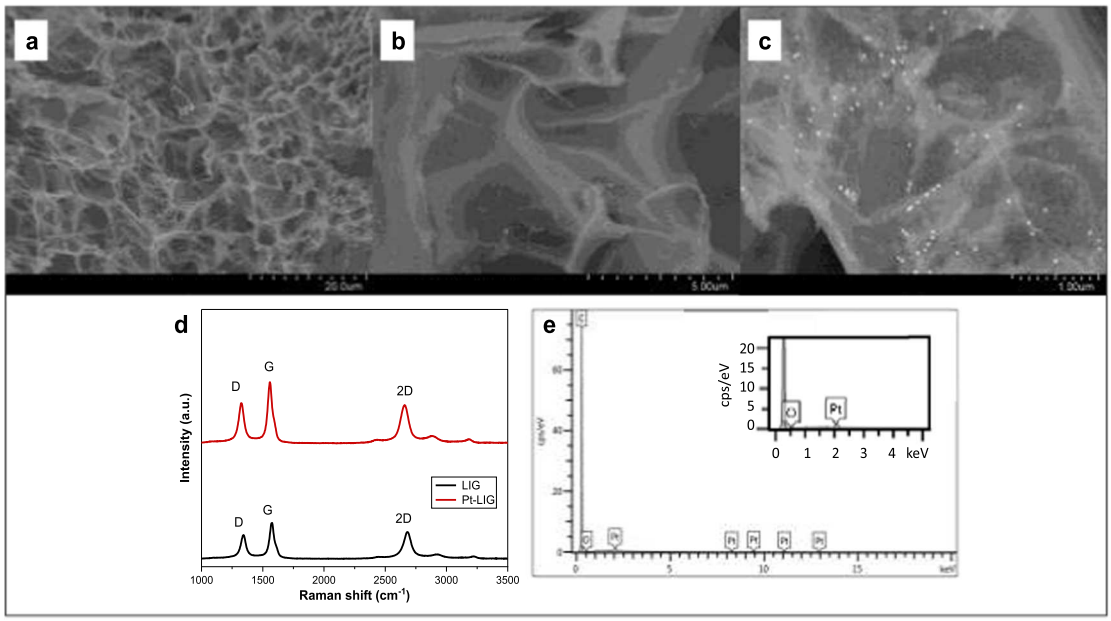

Figure 3. Characterization of the morphology and chemical composition of the Pt-LIG electrode loaded with 10 μg ml^{-1} of Pt NP. (a) FESEM image of electrode surface; (b) FESEM image at higher magnification revealing the distribution of Pt NPs; (c) Further magnification of FESEM showing Pt NPs associated with the walls of the porous LIG (d) Raman spectra of the Pt-LIG electrode compared to pristine LIG; (e) EDS analysis.

Table 2. Raman peak location and ratio.

	Peak Location (cm^{-1})			Peak Ratio	
Electrode	D	G	2D	I_D/I_G	I_{2D}/I_G
LIG	1343.29	1577.19	2680.63	0.67	0.74
Ag-LIG	1340.59	1574.58	2673.93	0.88	0.59
Pt-LIG	1324.38	1558.85	2658.27	0.88	0.87

both NP-LIG increased by 31.3%, suggesting the formation of new defects or the modification of existing ones due to the incorporation of NPs [37].

Interestingly, the I_{2D}/I_G ratio decreased for Ag-LIG but increased for Pt-LIG. This can be attributed to the presence of Ag introducing n-type doping effects on LIG which could change the electronic property of LIG and thereby affect the capacitance and sensing effectiveness of the electrode [38]. On the other hand, the increase of I_{2D}/I_G ratio on Pt-LIG may be explained by the smaller Pt-NPs effectively reduced the number of effective graphene layers on LIG due to changes in the graphene sheet stacking behavior [39] and possibly improving electronic conductivity. These structural and electronic modifications directly influenced the electrochemical behavior discussed in the subsequent sections.

The observations made from Raman analyses also suggest oxidation-related structural modification of LIG upon NP loading. The higher D-band intensity and redshift of both D and G peaks imply increased disorder and partial oxidation, which introduce additional oxygen-containing functional groups such as C–O and C=O. These groups enhance interfacial wettability and facilitate ion adsorption at the electrode–electrolyte interface, thereby improving double-layer capacitance and contributing to the enhanced electrochemical response observed in subsequent sections [40, 41].

3.2. Capacitance measurement

3.2.1. Influence of laser fabrication parameters on LIG capacitance

Figure 4 compares the capacitance of LIG electrodes fabricated under various laser powers, with and without NP loading. The capacitance of pristine LIG varied with fabrication power, which directly affects pore size, defect density, and sheet resistance, all key determinants of charge storage capacity [42].

After NP incorporation, changes in capacitance became strongly dependent on both the baseline morphology and the extent of NP interaction with the LIG surface. As seen in figure 4, electrodes fabricated at 16 W (fluence 37.58 J cm^{-2}) exhibited the most pronounced capacitance enhancement upon Ag-NP loading. This

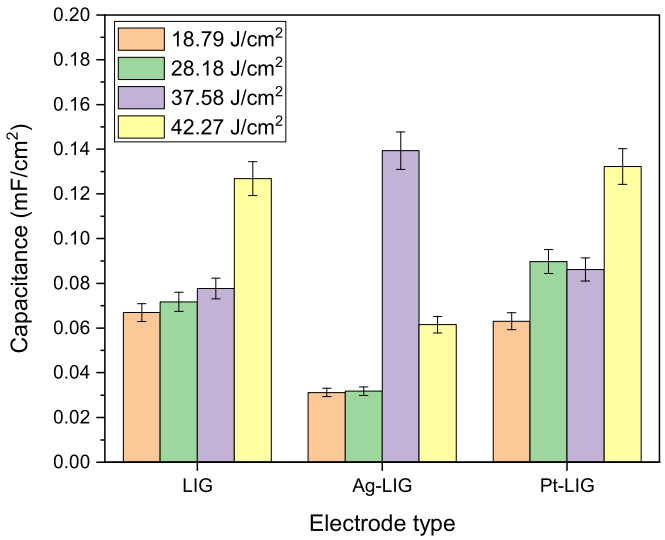

Figure 4. Capacitance comparison of LIG fabricated (average of three samples) at various laser fluences, with and without NP loading.

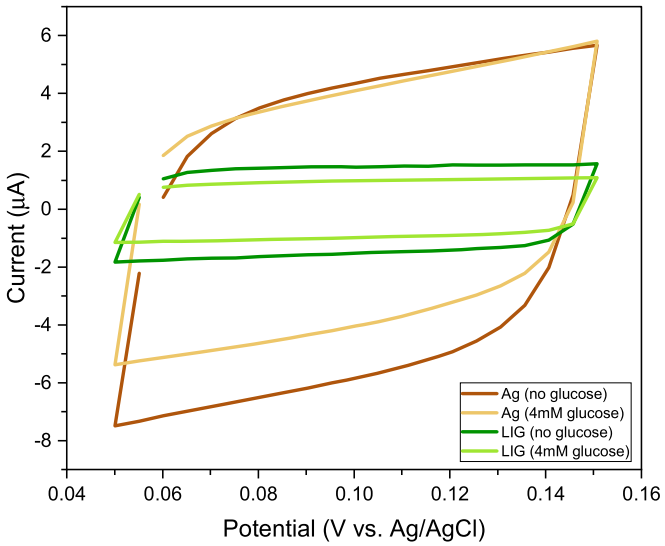

Figure 5. CV of LIG and Ag-LIG without glucose and with 4 mM glucose measured at 50 mV s^{-1}.

suggests an optimal balance between porosity and surface conductivity that facilitates both double-layer and faradaic charge storage.

The cyclic voltammetry (CV) curves at a scan rate of 50 mV s^{-1} shown in figures 5 and 6 depict the current response of the LIG with and without NP loading over a potential window. The area enclosed by the curve is indicative of the charge storage capacity, which is related to the capacitance and can be calculated by:

$$C = \frac{\int IdV}{s \cdot A \cdot \Delta V}$$

where I is the voltametric current, s is the voltage scan rate, A is the area of LIG immersed in the electrolyte, and ΔV is the potential window. Each data point represents the mean of three measurements, with standard deviations below 10%.

3.2.2. Comparative capacitive response of LIG and NP-LIG to glucose

The CV curve area of pristine LIG changed with the presence of 4 mM glucose, indicating a certain level of sensitivity towards glucose. The Ag-LIG electrode in figure 5 exhibits a more pronounced change in its CV curve upon the addition of 4 mM glucose compared to pristine LIG. The increase in the CV curve area indicates

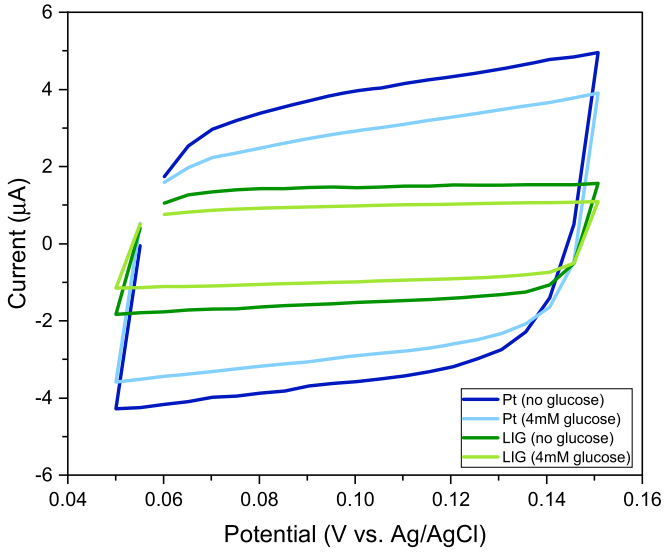

Figure 6. CV of LIG and Pt-LIG without glucose and with 4 mM glucose measured at 50 mV s^{-1}.

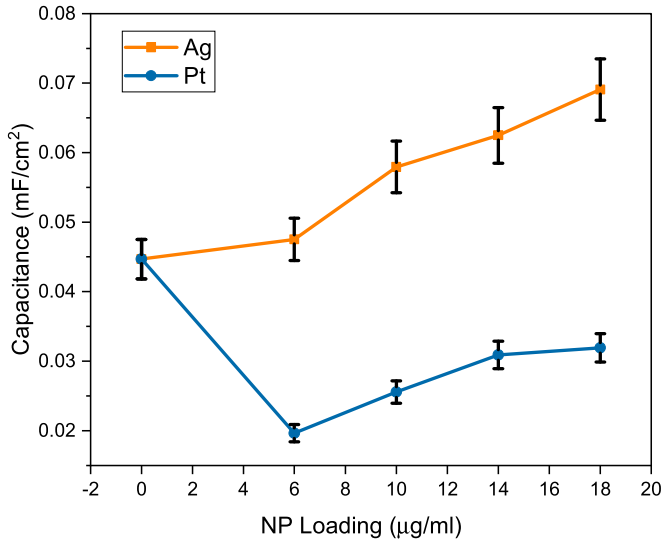

Figure 7. Capacitance of LIG at varied Ag and Pt NP loading measured at a scan rate of 50 mV s^{-1} with visual guide.

enhanced interaction with glucose molecules due to the presence of Ag NP [43]. This improved capacitive response is consistent with the oxidation-related features observed in the Raman spectra, where increased surface disorder and oxygen functionalities enhance the interaction between the LIG surface and glucose molecules, supporting more efficient charge transfer.

Similarly, in figure 6, Pt-LIG displayed a pronounced alteration in its CV response in the presence of glucose, confirming improved sensitivity due to the catalytic properties of Pt. Unlike Ag, Pt facilitates stronger adsorption and faster electron transfer during glucose oxidation, leading to improved surface reactivity and electrocatalytic efficiency. These observations indicate that both NPs contribute to the sensing functionality described in section 3.3 [44].

3.2.3. Effect of nanoparticle loading concentration on capacitance

Figure 7 illustrates the measured capacitance of LIG electrodes as a function of the loading concentration of both Ag and Pt NP, measured at a fixed scan rate of 50 mV s^{-1}. The capacitance of Ag-LIG increases continuously with increasing loading concentration up to 18 μg ml^{-1}.

In contrast, Pt-LIG showed no improvement at 6 μg ml^{-1}, with gradual enhancement at higher loadings up to 18 μg ml^{-1}. However, even at the maximum loading, its capacitance remained slightly lower than that of

pristine LIG. This behavior implies that Pt incorporation introduced additional structural strain, as indicated by the Raman redshift, partially offsetting its catalytic benefits.

At excessive NP loadings, both Ag and Pt electrodes exhibited slight performance decline, which can be attributed to NP agglomeration and partial pore blockage, which hindered ion accessibility and reduced effective surface area.

It is worth noting that only one NP size was used for each metal type (Ag ≈ 100 nm; Pt ≈ 30 nm) owing to cost and material availability considerations. This controlled approach ensured that variations in electrochemical response could be attributed primarily to differences in loading concentration rather than particle size effects.

3.3. Glucose sensitivity study

The LIG based electrode operates as a non-enzymatic glucose sensor, achieved through the direct electrochemical oxidation of glucose ($C_6H_{12}O_6$) at the catalytically active electrode surface. The glucose sensing mechanism for Ag-LIG are detailed as follows:

I. Oxidation of Ag in KCl electrolyte:

$$[Ag + Cl^- \rightarrow AgCl + e^-]$$
$$[2Ag + O_2 \rightarrow Ag_2O]$$

II. Glucose oxidation facilitated by Ag_2O to form gluconolactone:

$$[Ag_2O + HO_2 + e^- \rightarrow 2AgOH]$$
$$[AgOH + C_6H_{12}O_6 \rightarrow Ag + C_6H_{10}O_6 + H_2O + e^-]$$

III. Overall glucose detection reaction:

$$[Ag_2O + C_6H_{12}O_6 \rightarrow 2Ag + C_6H_{10}O_6 + H_2O + e^-]$$

The formation of gluconolactone ($C_6H_{10}O_6$) releases electrons which are then detected as an electrical current in electrochemical analysis. The reduction of Ag_2O back to Ag regenerates its catalytic activity for continuous glucose sensing. Similar processes take place for Pt-LIG in glucose sensing:

I. Oxidation of Pt in KCl electrolyte and in presence of water:

$$[Pt + Cl^- \rightarrow PtCl + e^-]$$
$$[Pt + H_2O \rightarrow PtO + 2H^+ + 2e^-]$$

II. Glucose oxidation facilitated by PtO to form gluconolactone:

$$[PtO + H_2O + e^- \rightarrow Pt(OH)_2]$$
$$[Pt(OH)_2 + C_6H_{10}O_6 \rightarrow Pt + C_6H_{10}O_6 + H_2O + e^-]$$

III. Overall glucose detection reaction:

$$[PtO + C_6H_{12}O_6 \rightarrow Pt + C_6H_{10}O_6 + H_2O + e^-]$$

The CV curves (figures 5 and 6) confirm that the incorporation of NP onto LIG enhances the electrode's response in the presence of glucose. As glucose concentration increased, both the CV curve area and peak current expanded more prominently for NP-LIG compared to pristine LIG, indicating improved sensitivity due to catalytic NP activity. This is in agreement with other NP-LIG based electrodes by other works in recent years, attributing to the enhanced catalytic properties by NP [8, 45, 46].

To eliminate baseline drift, the capacitance responses were normalized to the first five data points (figures 8 and 9). The sensitivity factor, derived from the slope of the linear region (figure 10), was used to compute the limit of detection (LOD) [47]:

$$LOD = \frac{3.3\sigma}{S_{slope}}$$

where σ is the standard deviation of response at 1M KCl without glucose (blank solution), and S_{slope} is the sensitivity factor from the calibration curve.

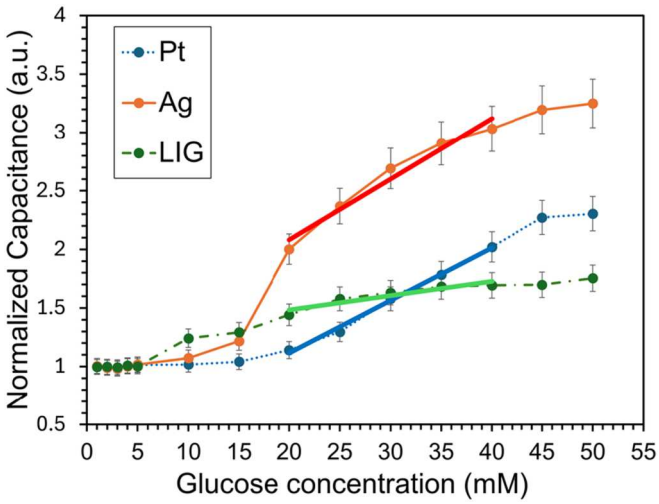

Figure 8. Capacitance response (with visual guide) of LIG with 10 μg ml^{-1} Ag and Pt NP measured at a scan rate of 5 mV s^{-1}.

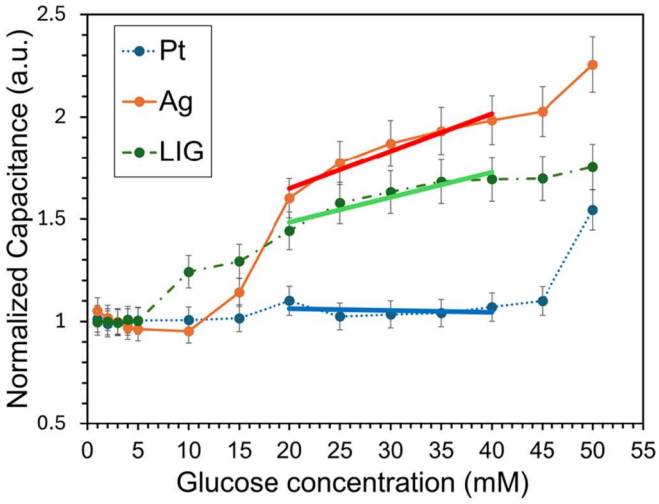

Figure 9. Capacitance response (with visual guide) of LIG with 18 μg ml^{-1} Ag and Pt NP measured at a scan rate of 5 mV s^{-1}.

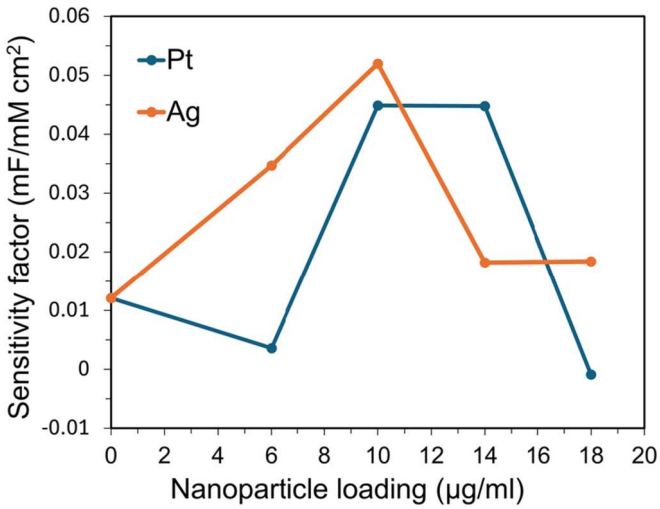

Figure 10. Sensitivity factor of Ag-LIG and Pt-LIG at different NP loading concentration to glucose.

Table 3. Comparison of the performances of LIG-Based sensors with various NP for glucose sensing.

Electrolyte	Electrode	Sensing mechanism	Sensitivity	Detection limit (μM)	Linear range	References
Artificial Saliva	Ag on LIG	Amperometry	24.1 μA $mM^{-1}\cdot cm^2$	45	1–2 mM	[37]
Sweat	Pt on LIG		4.62 μA $mM^{-1}\cdot cm^2$	0.3	0–2.1 mM	[38]
Glucose in Phosphate Buffer (pH 7)	Au on MWCNT		0.4 μA/mM	20	0.05–22 mM	[39]
Urine	Ni on LIG		57.99 mA $mM^{-1}\cdot cm^2$	0.0152	0.012–1.5 mM	[8]
Glucose in 0.1 M NaOH	Au-rGO-SWCNT		Not reported	0.0022	0–80 mM	[40]
Sweat	Au on LIG		1.2 mA $mM^{-1}\cdot cm^2$	1.5	0–30 mM	[41]
Blood serum	Cu on LIG		496 mA $mM^{-1}\cdot cm^2$	390	1 μM–6.0 mM	[15]
Glucose in 0.1 M NaOH	Ag NPs/f-GOx/GCE		2.94 μA μM^{-1}	0.001	0–28 μM	[6]
Glucose in Phosphate Buffer (pH 9)	PBA functionalized Graphene	Electrochemical capacitance/ impedance	0.43 % a.u. mM^{-1} (Baseline capacitance ~120 pF)	Not reported	0–27 mM	[42]
Glucose in Phosphate Buffer (pH 7, 4) and Human Serum	rGO + APBA		0.044 a.u. mM^{-1} (Baseline impedance 1172Ω)	0.1	0.1–50 mM	[43]
Glucose in 1M KCl solution	Pristine LIG		0.012 mF/mM·cm^2	7.6	20 mM–40 mM	This work
	Ag on LIG		0.052 mF/mM·cm^2	1.29	20 mM–40 mM	
	Pt on LIG		0.045 mF/mM·cm^2	2.68	20 mM–40 mM	

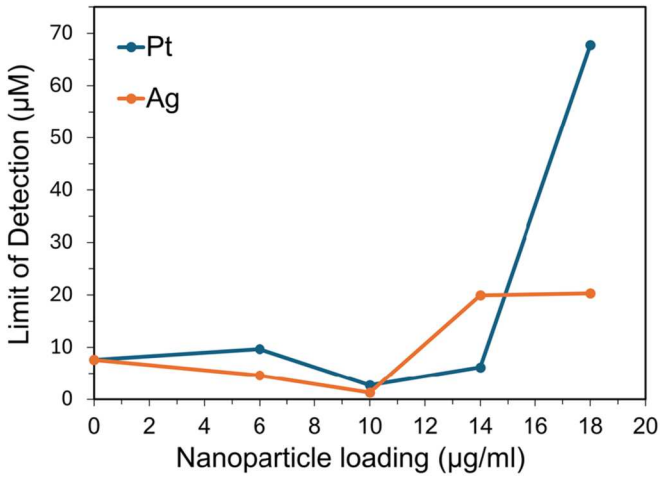

Figure 11. Limit of detection of Ag-LIG and Pt-LIG at different NP loading in glucose sensing.

The lowest LOD (1.29 μM) was obtained with 10 μg ml^{-1} of Ag loading on LIG (figure 11). This is a 52% improvement over Pt-LIG (2.68 μM) at the same loading concentration and a significant 83% improvement over pristine LIG (7.6 μM). At increasing loading concentration, the presence of Ag slightly improved the overall sensitivity towards glucose by enhancing the surface area of LIG and catalytic efficiency [48, 49]. Beyond the threshold of 10 μg ml^{-1}, the sensing performance of Ag-LIG dropped significantly. This can be due to the aggregation of the larger amount of Ag-NP, manifesting a physical barrier on the LIG surface and thus, hindering the adsorption of glucose molecules effectively [50].

Conversely, Pt-LIG at 6 μg ml^{-1} demonstrated reduced sensitivity towards glucose. This can be attributed to the enhancement of Pt-NP on LIG's catalytic properties being superior to that of Ag [51], where the strong adsorption of glucose molecules on the LIG surface may lead to a reduction in porosity and accessibility of activation sites, causing a decrease in overall capacitance and sensitivity towards glucose. A decrease in sensitivity was also observed for Pt-LIG at 18 μg ml^{-1}, similar to Ag-LIG, due to excessive NP aggregation, which is consistent with the observed high LOD.

Table 3 highlights that the proposed Ag-LIG system demonstrates competitive detection limits among recent LIG-based glucose sensors. While other works employ amperometry [20, 52–55] and electrochemical impedance [56, 57] for glucose detection, our work emphasises electrochemical capacitance as a viable alternative for non-enzymatic glucose sensing. Among many capacitive sensors, [58] reported a capacitive pressure-based glucose sensor using microbridge electrodes with limited focus on NP modified carbon surfaces while [59] introduced an advanced NP-functionalised graphene sensor optimized for micromolar glucose detection, our work uniquely targets high-concentration (gram-per-litre) industrial regimes using a flexible LIG base modified with Ag and Pt NP.

The incorporation of Ag NP in our electrode optimally enhances both capacitance and glucose sensitivity, which can be attributed to improved charge transfer at the electrode–electrolyte interface, increased accessible surface area for glucose adsorption, and the catalytic redox activity of Ag which facilitates efficient glucose oxidation and electron transport.

4. Conclusion

In this work, we demonstrated the enhancement of electrochemical capacitance-based glucose sensing performance by decorating LIG electrodes with metallic NPs. Comparative capacitive sensing analysis of pristine LIG with Ag and Pt loaded variants revealed that NP loading significantly increases the sensitivity and lowers the detection limit in a single-use non-enzymatic sensing configuration. The optimal loading concentration was identified to be 10 μg ml^{-1} for both Ag and Pt NP, achieving sensitivities of 0.0449 mF/mM·cm^2 and 0.052 mF/mM·cm^2, respectively - substantially surpassing that of pristine LIG. The lowest detection limit achieved was 1.29 μM for Ag-LIG, demonstrating strong potential for monitoring glucose concentrations releveant to industrial fermentation processes.

Performance degradation was observed beyond the optimal loading concentration, attributed to NP agglomeration and surface site blockage. This finding underscores the importance of balancing NP coverage to optimize catalytic enhancement while maintaining surface accessibility. As this study prioritized establishing

electrochemical performance and optimization of NP loading, FTIR analysis was reserved for subsequent work aimed at correlating surface chemistry with capacitive behavior. This future inclusion will strengthen understanding of oxidation effects and interfacial properties. To further explain interfacial charge-transfer dynamics, electrochemical impedance spectroscopy (EIS) is proposed for future work. This would help decouple double-layer capacitance and quantum capacitance contributions and provide insight into NP-LIG interfacial behavior under varying analyte concentrations. Overall, this study provides insight into the structure–property relationships of NP-LIG electrochemical interfaces, offering a cost-effective, flexible, and scalable platform for capacitive, non-enzymatic analyte detection. Future work will focus on real-time, in-line glucose sensing in food manufacturing environments to evaluate long-term stability and process integration potential, as well as expansion to include interference and selectivity tests for realistic fermentation and process monitoring conditions.

Acknowledgments

This work was supported by the Malaysian Ministry of Higher Education under (FRGS/1/2021/TK0/USMC/03/4). Part of this work was also supported by the UTM Fundamental Research Grant (Q.J130000.3823.23H25).

Data availability statement

All data that support the findings of this study are included within the article (and any supplementary files).

References

[1] Yang S *et al* 2022 Online glucose analysis system with high precision and wide detection range for fermentation monitoring *IEEE Trans. Instrum. Meas.* **71** 1–9
[2] Wang X, Liu T, Xue C, Wang Z and Sun X 2019 On-line monitoring of multiple component parameters during ethanol fermentation by near-infrared spectroscopy *Shengwu Gongcheng Xuebao/Chinese J. Biotechnol.* **35** 1491–9
[3] Pontius K, Semenova D, Silina Y E, Gernaey K V and Junicke H 2020 Automated electrochemical glucose biosensor platform as an efficient tool toward on-line fermentation monitoring: novel application approaches and insights *Front. Bioeng. Biotechnol.* **8** 1–15
[4] Wanjari V P, Reddy A S, Duttagupta S P and Singh S P 2023 Laser-induced graphene-based electrochemical biosensors for environmental applications: a perspective *Environ. Sci. Pollut. Res.* **30** 42643–57
[5] Gu C *et al* 2022 Experimental study on single biomolecule sensing using MoS2-graphene heterostructure nanopores *Nanoscale* **15** 266–74
[6] Feng Y, Liu Y, Feng B, Chen H, You L and Pei H 2021 Monitoring glucose in fermented beer by an electrochemical sensor based on graphene oxide decorated by silver nanoparticles *Int. J. Electrochem. Sci.* **16** 1–11
[7] Gao X, Du X, Liu D, Gao H, Wang P and Yang J 2020 Core–shell gold-nickel nanostructures as highly selective and stable nonenzymatic glucose sensor for fermentation process *Sci. Rep.* **10** 1–10
[8] Nugba B E, Mousa N O, Osman A and El-Moneim A A 2023 Non-enzymatic amperometric biosensor with anchored Ni nanoparticles for urinary glucose quantification *Diam. Relat. Mater.* **137** 110171
[9] Santos N F *et al* 2021 IR and UV laser-induced graphene: application as dopamine electrochemical sensors *Adv. Mater. Technol.* **6** 1–13
[10] Kulyk B *et al* 2021 Laser-induced graphene from paper for mechanical sensing *ACS Appl. Mater. Interfaces* **13** 10210–21
[11] Chen X, Gan K W, Pu S H, Jalalvand M and Hamilton A R 2025 Piezoresistive laser-induced graphene as a low-cost strain sensor for composite structures *Sensors Actuators A Phys.* **393** 116776
[12] Wang L, Wang Z, Bakhtiyari A N and Zheng H 2020 A comparative study of laser-induced graphene by co2 infrared laser and 355 nm ultraviolet (Uv) laser *Micromachines* **11** 1–9
[13] Stanford M G *et al* 2020 High-resolution laser-induced graphene. Flexible electronics beyond the visible limit *ACS Appl. Mater. Interfaces* **12** 10902–7
[14] Hristovski I R, Herman L A, Mitchell M E, Lesack N I, Reich J and Holzman J F 2022 Manifestations of laser-induced graphene under ultraviolet irradiation of polyimide with varied optical fluence *Nanomaterials* **12**
[15] Stanford M G, Yang K, Chyan Y, Kittrell C and Tour J M 2019 Laser-induced graphene for flexible and embeddable gas sensors *ACS Nano* **13** 3474–82
[16] Zhang Y *et al* 2020 A flexible non-enzymatic glucose sensor based on copper nanoparticles anchored on laser-induced graphene *Carbon N. Y.* **156** 506–13
[17] Sun X, Liu X, Xing X and Li F 2022 Electrodeposited with FeOOH and MnO2 on laser-induced graphene for multi-assembly supercapacitors *J. Alloys Compd.* **893**
[18] Rao Y, Yuan M, Luo F, Li H, Yu J and Chen X 2022 Laser In-Situ synthesis of metallic cobalt decorated porous graphene for flexible In-Plane microsupercapacitors *J. Colloid Interface Sci.* **610** 775–84
[19] Li L *et al* 2024 Laser-induced graphene decorated with MOF-derived NiCo-LDH for highly sensitive non-enzymatic glucose sensor *Molecules* **29**
[20] Aparicio-Martínez E P, Vega-Rios A, Osuna V and Dominguez R B 2023 Salivary glucose detection with laser induced graphene/AgNPs non-enzymatic sensor *Biosensors* **13** 1–13
[21] Sainz-urruela C, Vera-lópez S, Andrés M P S and Díez-pascual A M 2021 Graphene-based sensors for the detection of bioactive compounds: a review *Int. J. Mol. Sci.* **22**

[22] Goh R X, Sultan S M, Gan K W, Chong H M H, Pu S H and Ling T Y 2025 Flexible LIG-based breathing rate sensor with skin-contact recovery for smart masks using capacitive readout *11th Int. Symp. Sensors, Mechatronics Autom. Syst. ISSMAS 2025* 8–12
[23] Cai Y, Yang D, Yin R, Gao Y, Zhang H and Zhang W 2021 An enzyme-free capacitive glucose sensor based on dual-network glucose-responsive hydrogel and coplanar electrode *Analyst* **146** 213–21
[24] Slaughter G and Kulkarni T 2017 Highly selective and sensitive self-powered glucose sensor based on capacitor circuit *Sci. Rep.* **7** 1–9
[25] Batvani N, Alimohammadi S and Kiani M A 2022 Nonenzymatic glucose sensor design based on carbon fiber ultra-microelectrode: controlled with a manual micro adjuster *Anal. Chim. Acta* **1209** 339845
[26] Stoller M D *et al* 2011 Interfacial capacitance of single layer graphene *Energy Environ. Sci.* **4** 4685
[27] Zhan C, Neal J, Wu J and Jiang D E 2015 Quantum effects on the capacitance of graphene-based electrodes *J. Phys. Chem. C* **119** 22297–303
[28] Wu J 2022 Understanding the electric double-layer structure, capacitance, and charging dynamics *Chem. Rev.* **122** 10821–59
[29] Goh R X *et al* 2023 Effects of air exposure on the interfacial capacitance of laser-induced graphene (LIG) with and without silver (Ag) nanoparticle loading *IEEE Int. Conf. on Sensors and Nanotechnology (SENNANO)* 158–61
[30] Yoon Y *et al* 2015 Highly stretchable and conductive silver nanoparticle embedded graphene flake electrode prepared by *In situ* dual reduction reaction *Sci. Rep.* **5** 1–10
[31] Kartika A E, Setiyanto H, Manurung R V, Jenie S N A and Saraswaty V 2021 Silver nanoparticles coupled with graphene nanoplatelets modified screen-printed carbon electrodes for rhodamine b detection in food products *ACS Omega* **6** 31477–84
[32] Chiang Y C, Liang C C and Chung C P 2015 Characterization of platinum nanoparticles deposited on functionalized graphene sheets *Materials (Basel).* **8** 6484–97
[33] Björk J, Hanke F, Palma C A, Samori P, Cecchini M and Persson M 2010 Adsorption of aromatic and anti-aromatic systems on graphene through π-π Stacking *J. Phys. Chem. Lett.* **1** 3407–12
[34] Koniakhin S V, Utesov O I and Yashenkin A G 2024 Raman peak shift and broadening in crystalline nanoparticles with lattice impurities *Diam. Relat. Mater.* **146** 111182
[35] Zheng X *et al* 2015 The Raman redshift of graphene impacted by gold nanoparticles *AIP Adv.* **5**
[36] Mu Y *et al* 2023 Silver nanoparticles—laser induced graphene (Ag NPs—LIG) hybrid electrodes for sensitive electrochemical-surface enhanced Raman spectroscopy (EC-SERS) detection *Analyst* **148** 3087–96
[37] Mignoli T R, Hewer T L R, Antunes R A, Alves R M B and Schmal M 2021 Synthesis of few-layered graphene sheets as support of cobalt nanoparticles and its influence on CO hydrogenation *Mater. Sci. Eng. B Solid-State Mater. Adv. Technol.* **273** 115388
[38] Lee J, Novoselov K S and Shin H S 2011 Interaction between metal and graphene: dependence on the layer number of graphene *ACS Nano* **5** 608–12
[39] Muzyka K and Xu G 2022 Laser-induced graphene in facts, numbers, and notes in view of electroanalytical applications: a review *Electroanalysis* **34** 574–89
[40] Zuliani J E, Tong S, Jia C Q and Kirk D W 2018 Contribution of surface oxygen groups to the measured capacitance of porous carbon supercapacitors *J. Power Sources* **395** 271–9
[41] Cao H, Peng X, Zhao M, Liu P, Xu B and Guo J 2018 Oxygen functional groups improve the energy storage performances of graphene electrochemical supercapacitors *RSC Adv.* **8** 2858–65
[42] Lin J *et al* 2014 Laser-induced porous graphene films from commercial polymers *Nat. Commun.* **5** 12
[43] Bagheri R, Alikhani S and Miri-Moghaddam E 2023 Fabrication of conductive Ag/AgCl/Ag nanorods ink on Laser-induced graphene electrodes on flexible substrates for non-enzymatic glucose detection *Sci. Rep.* **13** 1–11
[44] Hoa L T, Sun K G and Hur S H 2015 Highly sensitive non-enzymatic glucose sensor based on Pt nanoparticle decorated graphene oxide hydrogel *Sensors Actuators, B Chem.* **210** 618–23
[45] Zhang Y, Zhang C, Chen W and Liu Z 2024 One-step laser-induced Cu-embedded graphene for non-enzymatic glucose sensing in beverages *J. Alloys Compd.* **992** 174563
[46] Jain A, Michalska M, Zaszczyńska A and Denis P 2022 Surface modification of activated carbon with silver nanoparticles for electrochemical double layer capacitors *J. Energy Storage* **54**
[47] Shrivastava A and Gupta V 2011 Methods for the determination of limit of detection and limit of quantitation of the analytical methods *Chronicles Young Sci.* **2** 21
[48] Movaghgharnezhad S and Kang P 2024 Laser-induced graphene: synthesis advances, structural tailoring, enhanced properties, and sensing applications *J. Mater. Chem. C* (https://doi.org/10.1039/d3tc04677j)
[49] Qu Z *et al* 2021 Porous carbon substrate improving the sensing performance of copper nanoparticles toward glucose *Nanoscale Res. Lett.* **16**
[50] Hu H, Li Y A, Liu M, Xu W and Zhou Y G 2025 Real-time, non-destructive monitoring of the aggregation behavior of silver nanoparticles using nano-impact electrochemistry *Nanoscale Horizons* (https://doi.org/10.1039/d5nh00019j)
[51] Guo C and Hu J 2014 Bimetallic alloy Pt/Ag nanoparticles with enhanced catalytic activity for formic acid oxidation *Appl. Phys. A Mater. Sci. Process.* **117** 809–13
[52] Yoon H *et al* 2020 A chemically modified laser-induced porous graphene based flexible and ultrasensitive electrochemical biosensor for sweat glucose detection *Sensors Actuators, B Chem.* **311** 127866
[53] Rakhi R B, Sethupathi K and Ramaprabhu S 2009 A glucose biosensor based on deposition of glucose oxidase onto crystalline gold nanoparticle modified carbon nanotube electrode *J. Phys. Chem. B* **113** 3190–4
[54] Luo Y, Kong F Y, Li C, Shi J J, Lv W X and Wang W 2016 One-pot preparation of reduced graphene oxide-carbon nanotube decorated with Au nanoparticles based on protein for non-enzymatic electrochemical sensing of glucose *Sensors Actuators, B Chem.* **234** 625–32
[55] Zhu J *et al* 2021 Laser-induced graphene non-enzymatic glucose sensors for on-body measurements *Biosens. Bioelectron.* **193** 113606
[56] Zhang Y, Ma R, Zhen X V, Kudva Y C, Bühlmann P and Koester S J 2017 Capacitive sensing of glucose in electrolytes using graphene quantum capacitance varactors *ACS Appl. Mater. Interfaces* **9** 38863–9
[57] Li S *et al* 2017 One step electrochemical deposition and reduction of graphene oxide on screen printed electrodes for impedance detection of glucose *Sensors Actuators, B Chem.* **244** 290–8
[58] Lakshmi G S and Rao K S 2024 Design of capacitive pressure sensor for continuous glucose monitoring system *Microsyst. Technol.* **30** 1581–91
[59] Che R *et al* 2026 Built-in capacitive biosensor based leveraging rolling circle amplification-architected bimetallic nanozyme/glucose oxidase catalytic forest for overcoming sensitivity limits in plant pathogen monitoring *Sensors Actuators B Chem.* **448**